Growth of tetragonal PtO by molecular-beam epitaxy and its integration into β-Ga_2O_3 Schottky diodes

Cite as: APL Mater. 13, 111108 (2025); doi: 10.1063/5.0274229
Submitted: 4 April 2025 • Accepted: 17 October 2025 •
Published Online: 13 November 2025

Felix V. E. Hensling,[1,2] Christopher T. Parzyck,[3,4] Bennett Cromer,[1] Md. Abdullah Al Mamun,[5] Y. Eren Suyolcu,[1,2] L. Kalaydjian,[2] Indra Subedi,[6,7] Jisung Park,[1] Kathy Azizie,[1] Qi Song,[1] Peter A. van Aken,[2] Nikolas J. Podraza,[6,7] Kyeongjae Cho,[5] Debdeep Jena,[1,8,9] Huili G. Xing,[1,8,9] Kyle M. Shen,[3,9] Darrell G. Schlom,[1,9,10] and Patrick Vogt[2,a)]

AFFILIATIONS

[1]Department of Materials Science and Engineering, Cornell University, Ithaca, New York 14853, USA
[2]Max Planck Institute for Solid State Research, Heisenbergstr. 1, 70569 Stuttgart, Germany
[3]Laboratory of Atomic and Solid State Physics, Cornell University, Ithaca, New York 14853, USA
[4]Stanford Institute for Materials and Energy Sciences, SLAC National Accelerator Laboratory, Menlo Park, California 94025, USA
[5]Department of Materials Science and Engineering, University of Texas at Dallas, Richardson, Texas 75080, USA
[6]Department of Physics and Astronomy, University of Toledo, Toledo, Ohio 43606, USA
[7]Wright Center for Photovoltaic Innovation and Commercialization, University of Toledo, Toledo, Ohio 43606, USA
[8]School of Electrical and Computer Engineering, Cornell University, Ithaca, New York 14853, USA
[9]Kavli Institute at Cornell for Nanoscale Science, Ithaca, New York 14853, USA
[10]Leibniz-Institut für Kristallzüchtung, 12489 Berlin, Germany

Note: This paper is part of the Special Topic on Ultrawide Bandgap Semiconductors.
[a)]**Author to whom correspondence should be addressed:** p.vogt@fkf.mpg.de

ABSTRACT

We demonstrate the epitaxial growth of tetragonal platinum monoxide (PtO) on MgO, TiO_2, and β-Ga_2O_3 single-crystalline substrates by ozone molecular-beam epitaxy. We provide synthesis routes and derive a growth diagram under which PtO films can be synthesized by physical vapor deposition. A combination of electrical transport and photoemission spectroscopy measurements, in conjunction with density functional theory calculations, reveal PtO to be a degenerately doped *p*-type semiconductor with a bandgap of $E_g \approx 1.6$ eV. Spectroscopic ellipsometry measurements are used to extract the complex dielectric function spectra, indicating a transition from free-carrier absorption to higher photon energy transitions at $E \approx 1.6$ eV. Using tetragonal PtO as an anode contact, we fabricate prototype Schottky diodes on *n*-type Sn-doped β-Ga_2O_3 substrates and extract Schottky barrier heights of $\phi_B > 2.2$ eV.

I. INTRODUCTION

In 1941, Moore and Pauling reported the crystal structure of tetragonal platinum monoxide (PtO) (space group: $P4_2/mmc$)[1]—and since then its existence has been debated.[2–6] This debate has been fueled by the high ionization potential and low electronegativity of platinum,[7] which prevented the epitaxial growth of tetragonal PtO until now. From a *growth perspective*, it is thus intriguing to demonstrate the possibility of oxidizing noble metals (such as platinum) by molecular-beam epitaxy (MBE) with such high ionization potentials and different low-energy bulk structures.[7,8]

Ultra-wide bandgap (UWBG) semiconductors are ushering in the next generation of high-power electronics, and β-Ga_2O_3 is *the*

archetypical new UWBG semiconductor with an extremely high Baliga figure-of-merit.[9–12] Its exceptionally high predicted breakdown electric field ($E_{max} \sim 8$ MV cm^{-1}) portends highly scalable power devices, and β-Ga_2O_3 is currently the only UWBG material with large-scale commercially available substrates, promising a low-cost and effective device platform.[13–15]

Essential electronic devices for efficient high-power conversion are rectifiers, such as the Schottky diodes. With an electron affinity of ~4 eV[16] and the absence of a *p–n* homojunction in β-Ga_2O_3, high Schottky barriers $\phi_B \approx 1.5$ eV on β-Ga_2O_3 were achieved using metals with high work functions: Ru, Ir, Pd, Pt, Ag, or Au.[17] To further increase ϕ_B, the noble-metal oxides IrO_2 and RuO_2 have recently been considered as anode materials, allowing $\phi_B > 1.5$ eV.[17,18]

To design efficient rectifiers for high-power switching processes, high-breakdown voltages with low leakage currents are required to minimize off-state power dissipation. In turn, high electrostatic Schottky barriers with $\phi_B > 2.2$ eV are needed to reach high electric fields ($E_{max} > 6$ MV cm^{-1}) at leakage currents of 1 mA cm^{-2}.[19] To date, existing Schottky junctions typically fail due to electric field crowding, which can be addressed by edge termination or by tolerating an exceedingly high leakage current at the Schottky interface.[19,20] From a *device perspective*, it is thus intriguing to grow epitaxial PtO on β-Ga_2O_3 in order to achieve $\phi_B > 2.2$ eV, potentially improving the device performance of Ga_2O_3-based Schottky diodes.[17,20–22]

Sputtered PtO_x has also attracted attention as an anode material for β-Ga_2O_3 as it leads to a higher $\phi_B \approx 2$ eV than is achievable by IrO_2, RuO_2, or PdO_x.[17,18] This Schottky barrier height is sufficient to outperform diodes made using other oxidized anode metal-contacts, e.g., the *p*-type oxide semiconductors NiO, SnO, or Cu_2O.[17,18,22–25] Unfortunately, sputtered PtO_x anode contacts in Schottky diodes possess non-uniform interface state densities at the β-Ga_2O_3 interface, leading to an increase in interface defects and eventually to premature device failure.[21,22]

In this work, we now introduce the growth of epitaxial tetragonal PtO on MgO, TiO_2, and β-Ga_2O_3 substrates using ozone MBE. This achievement allows us to thoroughly characterize this noble-metal oxide material by crystallographic, electric, spectroscopic, and optical analytic techniques. We analyze our PtO films *in situ* by reflection high-energy electron diffraction (RHEED) and *ex situ* by x-ray diffraction (XRD) and scanning transmission electron microscopy (STEM) to identify the existence of the tetragonal PtO phase.[1] Electrical resistivity and Hall measurements are used to obtain the electrical properties of tetragonal PtO. We use angle-resolved photoemission spectroscopy (ARPES) and density functional theory (DFT) to identify the full band structure of PtO. We apply spectroscopy ellipsometry to extract the near infrared to ultraviolet optical properties of PtO in the form of its complex dielectric function spectra to identify absorption features. We fabricate prototype Schottky diodes using PtO/β-Ga_2O_3 heterostructures and demonstrate the promise of epitaxial PtO as an anode material in next-generation β-Ga_2O_3-based high power devices.

The Schottky barrier height (ϕ_B) in the PtO/β-Ga_2O_3 heterostructure is obtained by employing three independent methods: (i) *T*-dependent capacitance–voltage (*C–V*), (ii) *T*-dependent forward current–density voltage (*J–V*), and (iii) *T*-dependent reverse leakage current–density surface electric field (*J–E*) measurements. To analyze these data, we next use four independent models: (i) standard *C–V* analysis for Schottky barriers that takes image-force-lowering (IFL) at high surface electric fields (E_{surf}) into account, (ii) a thermionic field-emission (TFE) current model, (iii) a thermionic emission (TE) current model, and (iv) a numeric Schottky barrier tunneling model that includes IFL. Combining all approaches and considering IFL, we extract an averaged Schottky barrier of $\phi_B^{avg} > 2.2$ eV for our PtO/β-Ga_2O_3 structure.

II. TETRAGONAL PLATINUM MONOXIDE (PTO)

A. Growth and structural characterization

The epitaxial synthesis of tetragonal PtO faces inherent challenges because platinum possesses a high oxidation potential, a high electronegativity, and multiple low-energy PtO_x structures.[6,7,26] Considering the maximum applicable ozone partial pressure in our MBE system of $P_{O_3} \approx 8 \times 10^{-6}$ Torr (i.e., 1×10^{-5} Torr of distilled ozone that is 80% ozone) and thermodynamic calculations performed by Shang *et al.*,[26] platinum may be able to reach its Pt^{2+} oxidation state (i.e., forming PtO) at $500 \lesssim T_G \lesssim 600$ °C and 10^{-6} Torr $\lesssim p_{O_3} \lesssim 10^{-5}$ Torr.

These thermodynamic expectations are summarized in the Ellingham diagram plotted in Fig. 1(a), describing the formation of PtO under MBE conditions.[26] An Ellingham diagram involves the determination of the Gibbs energy (ΔG) or oxygen pressure (P_{O_2}) as a function of *T*, for an oxidation reaction producing the desired product. In the present case, PtO is the stable phase at P_{O_2} sufficiently high to complete the reaction $Pt + \frac{1}{2}O_2 \rightarrow PtO$, but not so high as to complete the reaction $PtO + \frac{1}{2}O_2 \rightarrow PtO_2$.[26,30] These reactions form the boundaries of the yellow region shown in Fig. 1(a). An Ellingham diagram can be used to display the relative stability of a desired oxide compound, such as PtO. The oxidation potential lines with the ozone partial pressures (the dashed lines) depicted in Fig. 1(a) are obtained by

$$p_{O_2} = p_{O_3}^{2/3} \exp\left(\frac{\Delta G(T)}{RT}\right), \quad (1)$$

with molecular gas constant *R*. We use the ozone-to-oxygen conversion given in Refs. 27 and 28 and the experimental parameters provided in Sec. VIII A. The intersection of ozone oxidation potential lines (the dashed lines) with the yellow region in the Ellingham diagram in Fig. 1(a) provides guidance for the growth parameters needed to form PtO during ozone MBE.

Figure 1(b) investigates the 2-dimensional parameter space under which PtO can be formed. It depicts an experimental $P–T_G$ diagram for the epitaxial growth of PtO on MgO(001) [Fig. 2], TiO_2(110) [Fig. 4], and β-Ga_2O_3(010) substrates (supplementary material), and the growth windows under which the formation of PtO is possible. Note, the oxygen flux was provided by an oxidant P_{oxi} with 80% O_3 + 20% O_2 at background pressure (*P*). We find that platinum can only be oxidized to PtO at $P \approx 10^{-5}$ Torr and 420 °C $\lesssim T_G \lesssim$ 480 °C [the yellow area in Fig. 1(b)]. Data points of grown films are plotted as crosses, and the corresponding platinum or PtO phases are identified *in situ* by RHEED. This $P–T_G$ diagram can be divided into five major regimes: (i) the formation of amor-

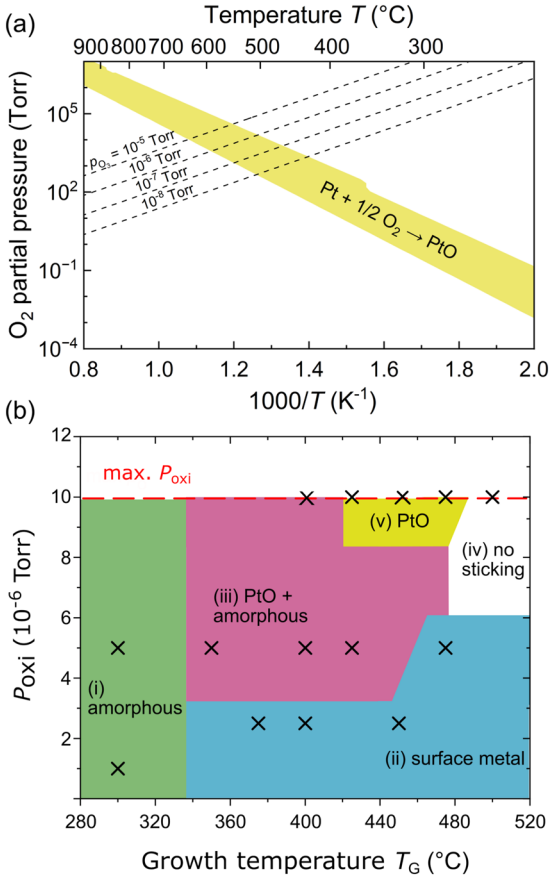

FIG. 1. (a) Ellingham diagram for the reaction Pt + $\frac{1}{2}$ O_2 → PtO (the yellow area). The calculation is taken from Ref. 26. The equilibrial oxidizing potential lines (the dashed lines) are calculated for ozone-to-oxygen conversion by Eq. (1) and using Refs. 27 and 28. (b) Growth diagram under which PtO film nucleation and subsequent film growth is feasible on MgO(001), TiO_2(110), and β-Ga_2O_3(010) substrates, projected onto the 2-dimensional parameter space spanned by the growth temperature (T_G) and background pressure (P_{oxi}) of the distilled ozone oxidant (80% O_3 + 20% O_2). Data points of grown films are depicted as crosses. The P_{oxi}–T_G diagram is divided into five major regimes, as indicated in the figure (details in the main text). The *growth window*, where the epitaxy of tetragonal PtO films becomes possible, is highlighted by the yellow area.

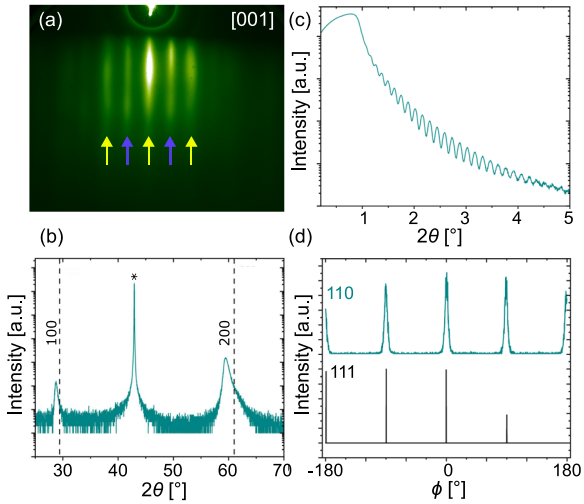

FIG. 2. (a) RHEED pattern of a PtO(100) film grown on a MgO(001) substrate taken along the [001] azimuth of the film. (b) Longitudinal XRD scan recorded for the same PtO film as shown in (a). The reflections of the film coincide with the tetragonal PtO phase grown with its (100) plane parallel to the (001) plane of the MgO substrate (marked by an asterix). (c) XRR of the same PtO film from which the film thickness of d = 60 nm was deduced. The clear Kiessig fringes confirm the uniform thickness of the PtO/MgO interface of this structure. (d) ϕ-scan along the 111 family of reflections of the MgO substrate (the black trace) at an off-axis angle χ = 54.74° and the 110 family of reflections of the PtO film (the green trace) at an off-axis angle χ = 45° imply the presence of 90° in-plane rotation twinning of the PtO film on the MgO(001) surface; see model in Fig. 3. The two twin domains give rise to the streaks arrowed in yellow and blue in (a).

phous PtO (the green area), (ii) the formation of metallic platinum (the blue area), (iii) the formation of mixed phases of crystalline PtO and amorphous PtO (the magenta area), (iv) the regime where PtO film nucleation is not possible, i.e., no sticking (the white area), and (v) the narrow MBE growth window under which epitaxial growth of PtO becomes feasible (the yellow area). We observe a similar behavior for the nucleation and growth of PtO on TiO_2 and β-Ga_2O_3; see the diffraction data in the supplementary material. The substrate surface dependence we observe is that PtO films on TiO_2(110) grow best at the lower T_G end of the growth window, PtO films on β-Ga_2O_3(010) only at the upper T_G end, while PtO films on MgO(001) grow best in the mid-T_G range of the identified growth window. Within experimental uncertainty, Fig. 1(a) and thermodynamical calculations[26] agree well with our identified PtO growth window displayed in Fig. 1(b).

Figure 2 shows diffraction data obtained on a PtO film grown on a MgO(001) substrate. Figure 2(a) shows the high surface crystallinity measured by RHEED along the [001] azimuth of the growing PtO film, and Fig. 2(b) shows a longitudinal XRD scan (i.e., a θ-2θ scan) of the same PtO film. Its peaks correspond to the (100) plane of PtO being parallel to the (001) plane of the MgO substrate. The asymmetry, especially observed for the 200 peak, is a sign of a partially relaxed film, giving rise to the range of out-of-plane lattice spacings comprising the observed 200 PtO peak. The Kiessig fringes observed at low diffraction angles during XRR measurements are seen in Fig. 2(c),[31] indicative of a film with a smooth surface and a flat film/substrate interface. Figure 2(d) shows an off-axis scan (i.e., a ϕ-scan) of the 110 family of peaks of the PtO film and the 111 family of peaks of the underlying MgO substrate, confirming the tetragonal crystal symmetry of PtO on MgO.[32] The four measured 110-type peaks of the PtO film, of which a PtO single crystal should have just two peaks, indicates the presence of 90° in-plane rotation twins in the epitaxial PtO film grown on the MgO(001) surface. This is also in agreement with the RHEED image in Fig. 2(a), which shows the emergence of additional streaks arising from two types of domains labeled D1 and D2 in the crystallographic model in Fig. 3. Domains D1 and D2 give rise to the streaks arrowed in yellow and blue in Fig. 2(a).

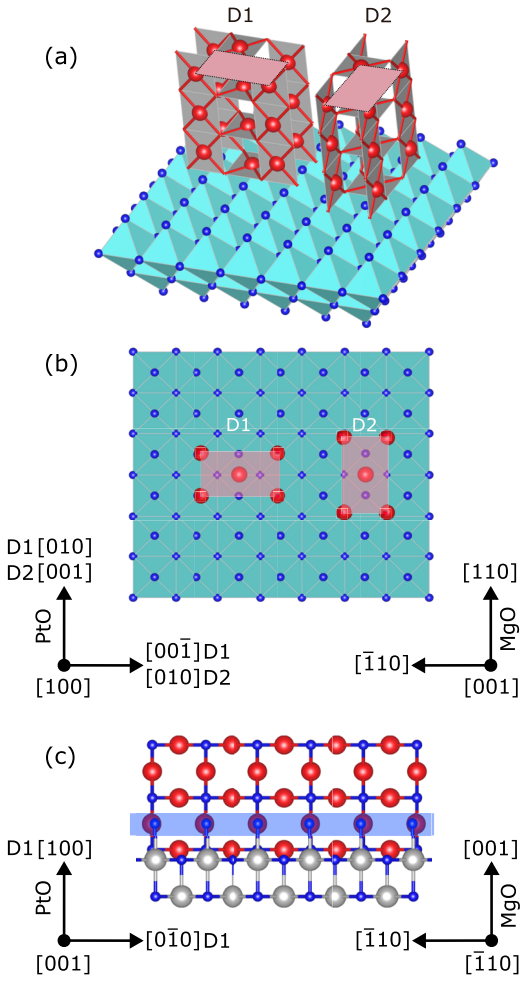

FIG. 3. Crystallographic model showing the observed orientation relationship between a tetragonal PtO film (space group: $P4_2/mmc$)[1] when grown on a cubic MgO substrate (space group: $Fm\bar{3}m$).[29] (a) Perspective view of the PtO(100)/MgO(001) heterostructure and 3-dimensional unit cells of both PtO twin domains (D1 and D2) and the MgO substrate. The polyhedral of PtO and MgO are depicted as gray and turquoise, respectively. (b) View along the [100] projection of the PtO film and [001] projection of the MgO substrate. The crystal orientations of both PtO domains (D1 and D2) and the MgO substrate are indicated. The surface unit cells of both PtO twins are highlighted by the red area. (c) Interface of a PtO(100)/MgO(001) heterostructure, explicitly modeled for D1 of the PtO film. The full epitaxial relationship is given in Eq. (2). Platinum, magnesium, and oxygen atoms are drawn in red, gray, and blue, respectively.

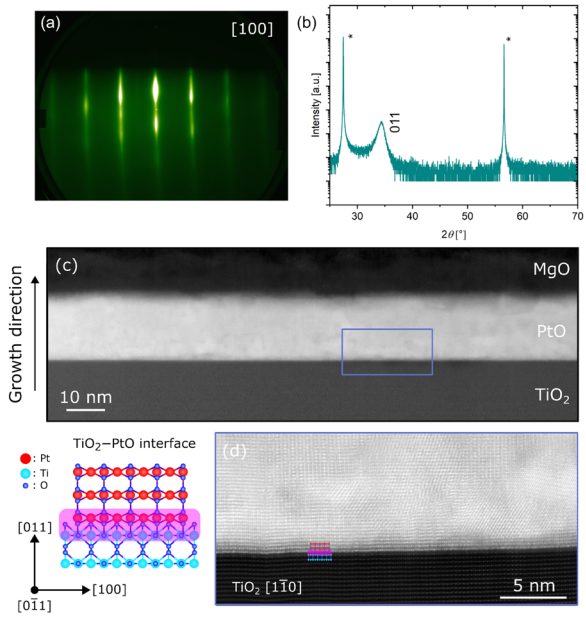

FIG. 4. (a) RHEED pattern of a PtO(011) film grown on a TiO_2(110) single-crystalline substrate, taken along the [100] azimuth of the PtO film. (b) Longitudinal XRD scan recorded for the same PtO film grown on TiO_2(110). The reflections of the PtO film coincide with the tetragonal PtO phase grown with its (011) plane parallel to the (110) plane of the TiO_2 substrate (marked by an asterix). (c) Low-magnification STEM-HAADF image taken along the [1$\bar{1}$0] zone axis of the TiO_2(110) substrate, presenting the overall quality of the MgO-capped epitaxial PtO film on TiO_2. (d) Higher-magnification STEM-HAADF image of area marked by the blue box Fig. 4(c), highlighting the PtO/TiO_2(110) interface with its structural model presented on the left-hand side. The epitaxial relationship of PtO(011)/TiO_2(110) is provided in Eq. (3).

In addition to the structural data and model obtained for PtO(100) grown on MgO(001) [Figs. 2 and 3], Fig. 4 shows RHEED, XRD, and scanning transmission electron microscopy high-angle annular dark-field (STEM-HAADF) analysis of PtO grown on a TiO_2(110) substrate. Figure 4(a) depicts the high surface crystallinity monitored by RHEED along the [100] azimuth of the growing PtO film. Figure 4(b) shows a longitudinal θ–2θ scan of the same PtO film grown on TiO_2(110). Its peaks correspond to the (011) plane of PtO being parallel to the (110) plane of the TiO_2 substrate. Further structural information is revealed by STEM-HAADF imaging at the nanoscale. STEM-HAADF images are presented in Figs. 4(c) and 4(d). Figure 4(c) presents the overall view of the complete PtO film grown on the TiO_2(110) substrate. High-magnification STEM-HAADF in Fig. 4(d) focuses on the interface of the PtO film and the TiO_2 substrate. The atomic-resolution image displays the interfacial connection in the first epitaxial monolayers and also demonstrates different nanosize domains in the upper part of the PtO film. This high-resolution STEM-HAADF image reveals an atomically abrupt interface of the grown PtO(011)/TiO_2(110) heterostructure, which though imperfect invites the investigation of PtO-based device structures such as the prototype PtO/β-Ga_2O_3 Schottky diodes studied in Sec. III.

Analyzing all data displayed in Figs. 2 and 4, we conclude that PtO crystallizes into its tetragonal polymorph with space group $P4_2/mmc$ as suggested in Ref. 1. Using stereographic projections, the epitaxial relationship of PtO on MgO is identified as

$$\begin{aligned} &\mathrm{MgO}(001) \parallel \mathrm{PtO}(100)\ (\text{out-of-plane})\ \text{with either} \\ &\mathrm{MgO}[110] \parallel \mathrm{PtO}[010]\ (\text{in-plane, D1})\ \text{or} \\ &\mathrm{MgO}[110] \parallel \mathrm{PtO}[001]\ (\text{in-plane, D2}). \end{aligned} \tag{2}$$

The epitaxial relationship of PtO(011)/TiO_2(110) is

$$\begin{aligned} TiO_2(110) &\parallel PtO(011), \\ TiO_2[1\bar{1}0] &\parallel PtO[0\bar{1}1], \\ TiO_2[001] &\parallel PtO[100]. \end{aligned} \tag{3}$$

We further suggest twinning of the PtO film grown on TiO_2 with the related epitaxial relationship as given in Eq. (3) of

$$\begin{aligned} TiO_2(110) &\parallel PtO(011), \\ TiO_2[1\bar{1}0] &\parallel PtO[01\bar{1}], \\ TiO_2[001] &\parallel PtO[\bar{1}00]. \end{aligned} \tag{4}$$

Twinning of this PtO film grown on TiO_2 has been observed by the twofold symmetric ARPES spectrum, plotted in Fig. 6.

The orientation relationship of the PtO(100) grown MgO(001) single-crystalline substrates is consistent with Ref. 32 for the growth of isostructural PdO(100) on MgO(001). The epitaxial relationship of PtO(011) grown on TiO_2(110) is consistent with the PtO(011)/TiO_2(110) interface displayed in Fig. 4(d), excluding the presence of the nanosized domains. The epitaxial PtO films grown on MgO, TiO_2, and β-Ga_2O_3 allow us to thoroughly analyze its electronic and optical properties and to determine the full band structure of tetragonal PtO. For this, electrical and Hall measurements and ellipsometry are performed.

B. Electrical transport measurements of PtO

Temperature-dependent electrical transport measurements were performed on PtO(100)/MgO(001) and PtO(011)/TiO_2(110) and are summarized in Fig. 5, with additional details provided in the supplementary material. The resistivity measurements shown in Fig. 5(a) demonstrate that the PtO films grown on MgO and TiO_2 exhibit weakly metallic behavior with residual resistivities between 0.8 mΩ cm ≤ ρ ≤ 1.0 mΩ cm. These values in ρ are similar to but slightly higher than the resistivity obtained by spectroscopic ellipsometry at room temperature shown in Fig. 7.

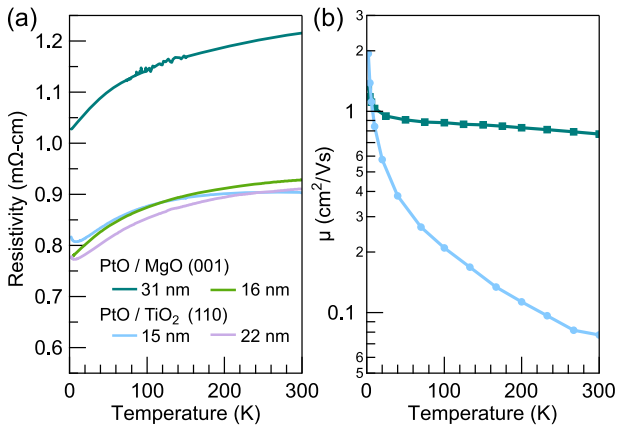

FIG. 5. Electrical properties of PtO films. (a) *T*-dependent resistivity of (uncapped) PtO films grown on MgO(001) and TiO_2(110) substrates. (b) *T*-dependent Hall measurements and obtained mobilities of PtO(100) and PtO(011) grown on MgO(001) and TiO_2(110) substrates, respectively.

Magnetic field-dependent measurements show only a weak, positive magneto-resistance at low-*T* on the order of 1%–2% at *T* = 2 K. Despite the marked similarity in the resistivity between films grown on the two substrates, the Hall resistance (ρ_{xy}) varies substantially between films synthesized on MgO and TiO_2. Temperature-dependent Hall measurements of PtO(100)/MgO(001) show linear behavior up to the highest magnetic fields of *H* = 7 T and down to *T* = 2 K. In contrast, a nonlinear component of ρ_{xy} is apparent in PtO(011)/TiO_2(110) below *T* < 6 K. For PtO films grown on MgO and TiO_2 substrates, a strictly positive hall coefficient was obtained at all temperatures (supplementary material)—consistent with PtO being a *p*-type semiconductor. We speculate that excess oxygen in our PtO films, i.e., $PtO_{1+\delta}$, leads to the measured *p*-type conductivity. In addition, the measured carrier concentrations *N* for films on the two substrates differ substantially at room temperature: $N \approx 3 \times 10^{21}$ cm^{-3} for PtO(100)/MgO(100) and $N \approx 1.3 \times 10^{23}$ cm^{-3} for PtO(011)/TiO_2(110). This difference in the Hall resistance coupled with similar values of ρ_{xx} manifest in different estimates of the *T*-dependent hole mobility μ for films on the two substrates as shown in Fig. 5(b). Between the two, the PtO film on MgO (001) exhibits a superior room-temperature mobility of $\mu \approx 0.8$ cm^2 V^{-1} s^{-1}. However, we note that more studies on epitaxial PtO are needed to determine whether stoichiometric PtO will be insulating, which would agree with our observed p-type conduction in our epitaxial PtO films, or if PtO might be semimetallic instead.[68]

C. Band structure and electronic properties of PtO

The synthesis of epitaxial, tetragonal PtO on MgO and TiO_2 substrates enabled us to investigate its full electronic and band structure using photoemission spectroscopy. Figure 6 summarizes both the calculated and measured electronic structures of PtO on TiO_2(110). Angle integrated ultraviolet photoemission spectra (UPS) are reported in Fig. 6(a), providing a measure of the occupied density of states (DOS). In spectra taken with two incident photon energies ($h\nu$ = 21.2 eV and $h\nu$ = 40.8 eV) a clear step is apparent at the Fermi energy E_F, consistent with the metallic behavior observed in resistivity measurements (Fig. 5). Most prominently, two sets of peaks are visible just below E_F, with binding energies spanning from 0 to 4 and 4–10 eV. Comparing these spectra to the orbitally projected DOS, and calculated using DFT, we identify the peaks at lower binding energies (0–4 eV) with states of primarily Pt 5*d* character, mixed with a minority of Pt 5*s* and O 2*p* weight. The higher energy manifold (5–10 eV) corresponds to a roughly equal mixture of O 2*p* and Pt 5*d* states. Finally, we observe a small feature at a binding energy of 22 eV which can be associated with the O 2*s* core level.

Overall, the experimental DOS probed by UPS agrees well with the DFT calculations modulo shift in E_F below the valence band maximum by 1.3 eV. This shift in E_F corresponds to the removal of roughly $0.67e^-$ per unit cell, i.e., 0.33 holes per platinum atom, and a hole doping of ~10^{22} cm^{-3}—consistent with the low temperature Hall measurements. While ultraviolet photoemission measurements were not performed on PtO(100)/MgO(001) samples, the results described here are quantitatively consistent with the lower energy resolution XPS measurements of the valence states reported for a sample on MgO, provided in the supplementary material.

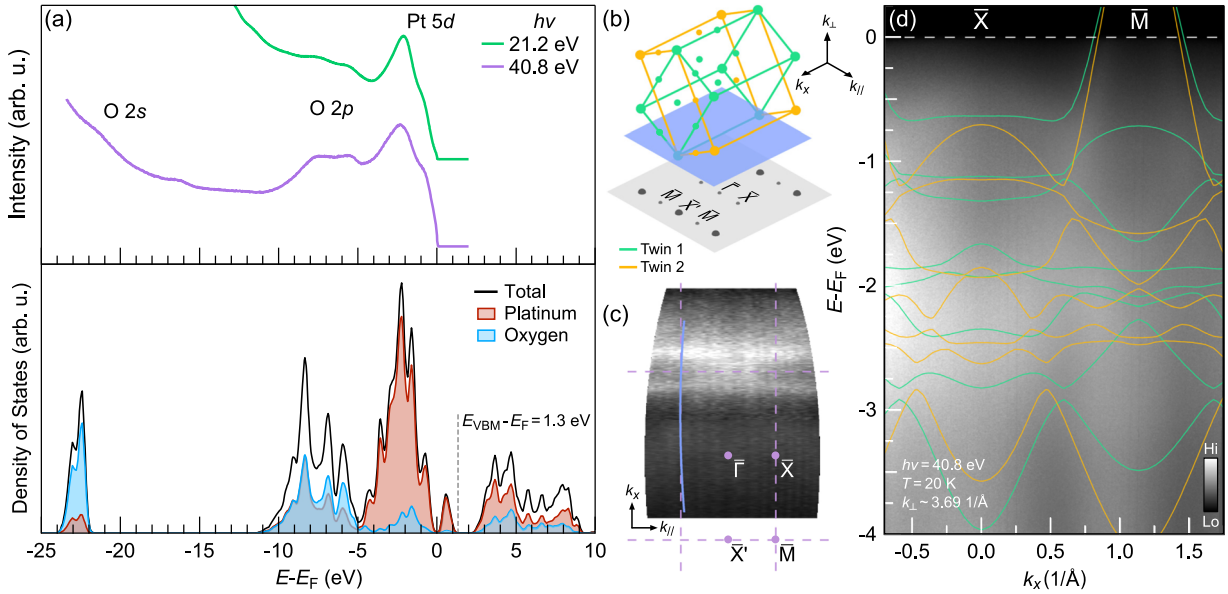

FIG. 6. Photoemission spectroscopy measurements of the same epitaxially grown PtO(011) film on a TiO_2(110) substrate as shown in Fig. 4. (a) Angle-integrated photoemission spectra taken with He-I light ($h\nu$ = 21.2 eV) and He-II light ($h\nu$ = 40.8 eV) along with the DFT-calculated density of states (DOS) projected onto the Pt *d* and O *s*, *p* orbitals. The results of the DOS calculation have been shifted by $E_{VBM} - E_F$ = 1.3 eV to match the peak positions in the measured spectra above. (b) Schematic of the Brillouin zones of two 180°-rotated twin domains of (011)-oriented PtO (yellow, green) with the high symmetry points marked the projected zone below (gray). In this schematic, k_x is taken to be along PtO(100) and $k_\perp$ along PtO(011). The approximate location (in momentum space) of ARPES spectra taken with He-II light are indicated by the blue plane. (c) Fermi surface map ($E = E_F \pm 50$ meV) of a PtO(011) film taken with He-II light and the spectrometer slit aligned along TiO_2[001]. High symmetry lines and points of the projected 2D-zone for twin 1 with PtO[100]‖TiO_2[001] are marked in purple. (d) ARPES spectrum taken with $h\nu$ = 40.8 eV through the path in momentum space indicated by the blue line in (c). The DFT-calculated band structure at the estimated out-of-plane momentum ($k_\perp$ = 3.69 Å^{-1}) is overlaid with bands originating from the two twin domains colored in green and yellow.

In addition to UPS measurements, the surface quality of the MBE-grown films is also sufficient to permit ARPES measurements of the electronic structure. In Figs. 6(c) and 6(d), we report angle-resolved spectra taken with Helium II light ($h\nu$ = 40.8 eV) and with the spectrometer slit aligned along TiO_2[001]. The Fermi surface map ($E = E_F \pm 50$ meV) shown in Fig. 6(c) exhibits a twofold symmetry about the $k_\parallel$ = 0 plane, consistent with the presence of 180°-rotated twins (T1 and T2), see the epitaxial relationship of PtO(011)/TiO_2(110) provided in Eqs. (3) and (4). In the calculations and analysis that follow, we will consider these twins when analyzing the spectra. The presence of these twins, T1 and T2, means that the ARPES measurement should reflect a mixture of signals from two reflected Brillouin zones, as pictured by the green and yellow wireframes in Fig. 6(b), respectively. This doubling of the bands, combined with the tilt of the principal axes and the measurement geometry, complicates the precise determination of measurement location in reciprocal space, specifically along the out-of-plane coordinate $k_\perp$. A comparison of ARPES spectra obtained with multiple incident energies $h\nu$ = 21.2 eV and $h\nu$ = 40.8 eV to DFT calculations yield an estimate of the inner potential V_0 between 13 and 17 eV. We refer to the reader to the supplementary material for a discussion of this procedure. Based on this estimate, the out-of-plane momentum probed with $h\nu$ = 40.8 eV is roughly 3.56 Å^{-1}. This is represented by the blue plane intersecting the two zones in Fig. 6(b).

Figure 6(c) shows a Fermi-surface map ($E = E_F \pm 50$ meV) taken at this nominal out-of-plane momentum. The primary feature is a pair of pockets located at the zone edge about the $\bar{M}$ points. While these pockets appear disconnected when measured with He-II light, they manifest as a single continuous feature covering the extent of the Brillouin zone edge when measured at a different $k_\perp$ using He-I light ($h\nu$ = 21.2 eV). An energy-momentum cut taken in the k_x direction through the $\bar{M}$ point is shown in Fig. 6(d), and indicated by the blue curve in Fig. 6(c). At this value of $k_\perp$, a cut through $\bar{M} - \bar{X} - \bar{M}$ nearly coincides with the M–X–M line, though it is slightly off the high-symmetry path in $k_\perp$. In this spectrum, there are two clear, nearly linearly dispersing bands which cross E_F about the $\bar{M}$-point and form the hole-like pocket observed in the map. By comparing to a DFT calculation of the band structure at $k_\perp$ = 3.69 Å^{-1} (green and yellow traces) shifted by the same value obtained from the analysis of the UPS and DOS ($E_F = E_{VBM} - 1.3$ eV), we identify these features as the light-hole bands. Evidently, at this photon energy (and in measurements with $h\nu$ = 21.2 eV), the so-called heavy-hole bands do not appear. We note, however, that based on the estimated shift in the Fermi level, they remain partially filled (though mostly depleted) and cross below E_F at values of $k_\perp$ not sampled by the photon energies utilized in this study.

Comparison of the DFT band structure and measured dispersion at two different values of $k_\perp$ (supplementary material) show good agreement with only a rigid shift of the bands to account for

the substantial hole doping in the sample. No additional renormalization of the bandwidth was required for good agreement between the ARPES and DFT. This indicates that the HSE06 calculations with mixing parameter of $\alpha = 0.33$ well describe the electronic structure of the tetragonal PtO films.

D. Optical properties of PtO

Accurate optical characterization of the PtO film is of critical importance, particularly when integrated into a device structure (Fig. 8). To obtain this, we use spectroscopic ellipsometry to measure and determine the complex dielectric function ($\epsilon = \epsilon_1 + i\epsilon_2$), absorption coefficient (α), and optical spectra of the PtO grown on MgO.

For the uncoated MgO single crystal, the structural model consists of a semi-infinite (1.98 ± 0.02) nm surface layer and ambient air. The complex dielectric function spectra for MgO can be represented by a Sellmeier expression.[33,34] Spectra in ϵ of the surface layer are represented by a Bruggeman effective medium approximation consisting of equal parts bulk MgO and air ambient.[35,36] Resulting fit parameters are reported in Table II.

The structural models of uncapped PtO consist of a semi-infinite MgO substrate, an epitaxial PtO film, and ambient air. The structural models of capped PtO consist of a semi-infinite MgO substrate, an epitaxial PtO film, and a thin MgO capping layer. Spectra in ϵ obtained from the uncoated MgO single crystal are used to represent both the substrate and capping layer (not shown). The ellipsometric spectra for two uncapped and two capped PtO films are fitted simultaneously in a multiple sample analysis with epitaxial PtO and MgO capping layer thicknesses as independent fitting parameters using common spectra in ϵ.

The parameterization for spectra in ϵ for PtO consists of (i) a constant additive term ϵ_∞, (ii) a Sellmeier expression,[33,34] (iii) a Drude expression describing the free-carrier concentration,[37] and (iv) four Lorentz oscillators, describing higher energy absorption features.[34] The resulting sum is explicitly given in Eq. (A1). This parametric model is obtained for all samples simultaneously and is shown in Fig. 7, with parameters collected in Table III. After determining the structural properties from this multiple sample analysis, layer thicknesses are fixed for each sample and spectra in ϵ are obtained independently using numerical inversion.[38] Figure 7 shows PtO spectra in ϵ obtained for each sample and the corresponding absorption coefficient,

$$\alpha = \frac{4\pi k}{\lambda}, \tag{5}$$

with photon wavelength λ and extinction coefficient k obtained from $\epsilon = (n' + ik)^2$ with refractive index n'. The magnitude of ϵ_2 and α indicates that the PtO film is heavily absorbing over the measured spectral range and ϵ_D [Eq. (A1)] yields $\rho = (0.74 \pm 0.01)$ mΩ cm. This value of ρ is similar but slightly lower than the resistivity obtained by electrical measurement in Fig. 5. This difference is reasonable as the electric fields of the probing ellipsometer beam (over this spectral range) oscillate at much higher frequencies than those of the direct electrical measurement. Thus, extending the spectral range to lower photon energies typically leads to better convergence between optically determined resistivity and direct electrical measurements.[39] Minima are observed in both ϵ_2 and α, indicating a transition in dominance between ϵ_D (describing free-carrier absorption) and ϵ_L (describing higher energy electronic transitions). For α obtained by multiple sample analysis and numerical inversion, the minima are located between $1.50\ \text{eV} \le E \le 1.62\ \text{eV}$. In this range, the magnitude $\alpha > 10^5\ \text{cm}^{-1}$ is too high for extrapolating an optical gap; thus, the minima in α are treated as proxies for the energy gap (E) between free-carrier absorption and higher energy, more tightly bound transitions. After characterizing our PtO films by crystallographic, transport, and optical measurements, we next integrate PtO as anode material on semiconducting n-type β-Ga_2O_3.

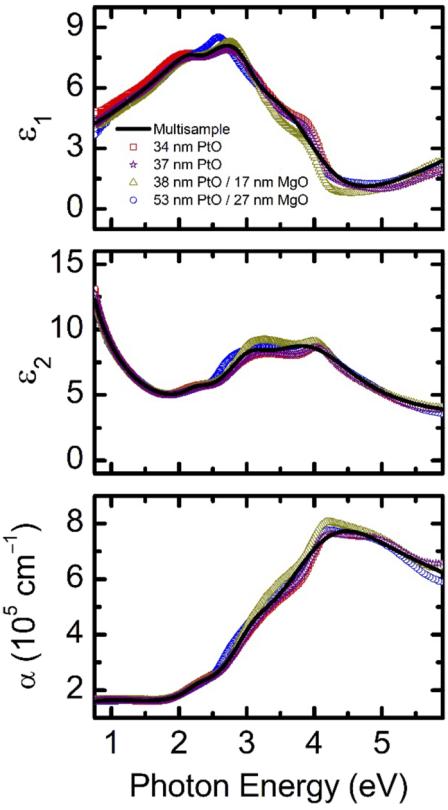

FIG. 7. Complex dielectric function ($\epsilon = \epsilon_1 + i\epsilon_2$) and absorption coefficient (α) spectra obtained for PtO using a multiple sample analysis (solid lines) and numerical inversion for each sample (symbols). The model and obtained parameters are given by Eq. (A1) and in Table III.

III. β-Ga_2O_3 SCHOTTKY DIODE USING PTO AS ANODE

To design vertical Schottky diodes for high-power switching, high breakdown voltages with low leakage currents are required, to minimize off-state power dissipation and to avoid premature device failure. In existing β-Ga_2O_3 Schottky diodes, the blocking voltage is often limited by the reverse leakage current. Thus, minimizing the Schottky barrier tunneling current requires maximizing the Schottky barrier height, i.e., $\phi_B > 2.2$ eV.[19,40]

Owing to the large electron affinity of β-Ga_2O_3, large ϕ_B can be achieved using noble-metal oxides as anode contacts (see Sec. I).[17]

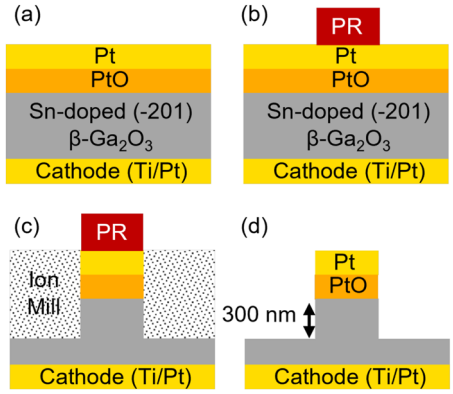

FIG. 8. Schematic process flow for a vertical Pt/PtO/β-Ga_2O_3 Schottky diode: (a) the as-grown Pt/PtO/β-Ga_2O_3/Ti/Pt structure, (b) photolithographic definition, (c) self-aligned mesa isolation by ion-milling, resulting in (d) mesa-height of 300 nm.

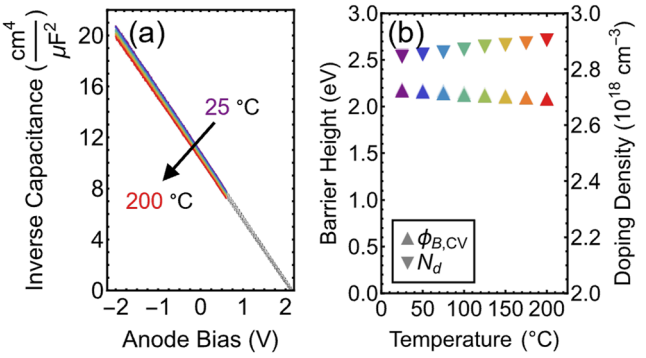

FIG. 9. (a) *T*-dependent *C*–*V* characteristics of the PtO/β-Ga_2O_3 Schottky diode fitted by Eq. (6). (b) Extracted values of the Schottky barrier ($\phi_{B,CV}$) and net doping (N_d) obtained using Eqs. (7) and (8). The color of the *T*-dependent data plotted in (a) follows the corresponding temperature color scale used in (b).

The successful integration of IrO_2 and RuO_2 on β-Ga_2O_3 has been recently achieved by Cromer *et al.* using ozone MBE.[18]

Following this approach, we use our PtO/β-Ga_2O_3 structure to process Schottky diodes, now using epitaxially grown tetragonal PtO as the anode contact (supplementary material). The schematics and processing are depicted in Fig. 8. For this structure, we extract ϕ_B as a function of T, characterized by three independent measuring methods: (i) T-dependent capacitance–voltage (C–V), (ii) T-dependent forward current–density voltage (J–V), and (iii) T-dependent reverse leakage current–density surface electric field (J–E) measurements.

The standard C–V extraction for a Schottky barrier height is[41]

$$\frac{1}{C^2} = -\frac{2}{qN_d\varepsilon_s a^2}(V_{BI} - V_F), \tag{6}$$

with the measured capacitance C, electron charge q, net doping density N_d, low-frequency permittivity $\varepsilon_s = 10\varepsilon_0$ of β-Ga_2O_3,[42] anode area a, built-in voltage V_{BI}, and forward bias voltage V_F. Including corrections for the Fermi energy (ΔE_F) and image-force lowering ($\Delta\phi_{IFL}$), ϕ_B can be extracted by[13]

$$V_{BI} = \phi_B - \Delta E_F + \Delta\phi_{IFL}. \tag{7}$$

At high surface electric fields E_{surf}, large ϕ_B, and large N_d, image-force lowering becomes *non*-negligible, expressed as[43]

$$\Delta\phi_{IFL} = \sqrt{\frac{qE_{surf}}{4\pi\varepsilon_s}} \propto \sqrt{E_{surf}} \quad \text{with}$$
$$E_{surf} = \sqrt{\frac{2qN_d(\phi_B + V_R)}{\varepsilon_s}} \propto \sqrt{\phi_B N_d} \tag{8}$$

and reversed bias voltage V_R.

Equations (6)–(8) are applied to the C–V data plotted in Fig. 9(a) to obtain ϕ_B and N_d as a function of T, which are plotted in Fig. 9(b). Values for the C–V Schottky barrier height and doping density for PtO/β-Ga_2O_3 diodes are given in Table I. The measured values on heating and cooling are essentially coincident with the values for cooling represented as opaque symbols. The monotonic decrease in the effective ϕ_B is consistent with prior reports and attributed to a reduction in the effective bandgap of β-Ga_2O_3.[13,18,19] As this reduction primarily occurs within the conduction band, increasing T effectively raises the conduction band minimum and thus reduces V_{BI}.

TABLE I. Extracted and averaged ϕ_B and N_d values obtained over the measured T-range using: (i) Standard C–V [Eq. (6)], (ii) thermionic field-emission (TFE) current [Eq. (9)], (iii) thermionic (TE) current [Eq. (12)], and (iv) reverse leakage current (RIV) [Eq. (14)]. The averaged values given here are obtained from the data plotted in Figs. 9–11.

Method	ϕ_B (eV)	N_d (10^{18} cm^{-3})
C–V	2.2 ± 0.1	2.9 ± 0.1
TFE	2.5 ± 0.1	⋯
TE	1.7 ± 0.2	⋯
RIV	2.0 ± 0.1	⋯

The forward bias characteristics can be described by (i) the thermionic field-emission (TFE) current,

$$J_{TFE} = \frac{A_R T\sqrt{\pi E'}}{k_B \cosh\left(\frac{E'}{k_B T}\right)}\sqrt{(\phi_B - \Delta\phi_{IFL} - \Delta E_F - qV_F)} \times \exp\left(-\frac{\Delta E_F}{k_B T}\right)\exp\left(-\frac{\phi_B - \Delta\phi_{IFL} - \Delta E_F - qV_F}{E''}\right), \tag{9}$$

with the Richardson constant $A_R = 4\pi m^* k_B q h^{-3}$,[44] the Boltzmann constant k_B, characteristic energy terms,[45]

$$E' = \frac{q\hbar}{2}\sqrt{\frac{N_d}{m^*\varepsilon_s\varepsilon_0}},$$
$$E'' = E' \coth\left(\frac{E'}{k_B T}\right), \tag{10}$$

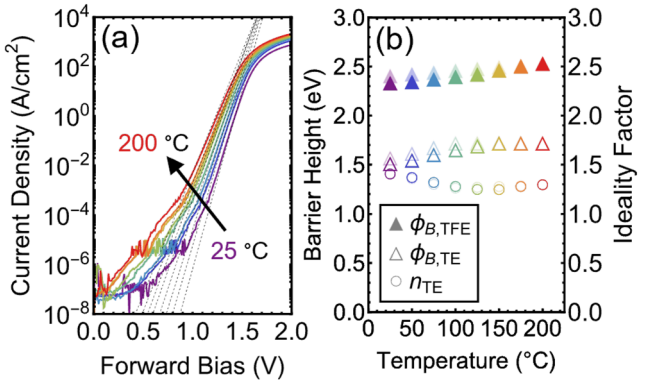

FIG. 10. (a) *T*-dependent forward *J*–*V* characteristics for the PtO/β-Ga_2O_3 Schottky diodes overlaid with the TFE current model, Eq. (9). (b) Extracted ϕ_B and *n* as a function of *T* by applying Eq. (9) (filled symbols) and Eq. (12) (hollow symbols) to the data. The color of the *T*-dependent data plotted in (a) follows the corresponding temperature color scale used in (b).

the electrons effective mass m^*, and the relative permittivity ε_r of β-Ga_2O_3.[46] The doping concentration is now given by

$$N_d = N_c \frac{2}{\sqrt{\pi}} F_{\frac{1}{2}}\left(-\frac{\Delta E_F}{k_B T}\right), \tag{11}$$

with the Fermi–Dirac integral of order $\frac{1}{2}$ $F_{\frac{1}{2}}$ and the effective DOS at the conduction band edge N_c.

Using N_d obtained from *C*–*V* measurements (Fig. 9), ϕ_B is the only free parameter when fitting the data plotted in Fig. 10(a) by Eqs. (9) and (10). The resulting values of ϕ_B are shown as a function of *T* in Fig. 10(b). The averaged barrier height extracted from this TFE model is given in Table I. We note that the PtO anode retains a high barrier height $\phi_B > 2.2$ eV on heating and cooling. This is initial evidence that no phase change occurred during measurement at elevated *T* due to reduction nor thermal decomposition. This apparent reduction was previously observed in AuO_x and AgO_x, which degraded on heating to values comparable to their respective plain metal contacts.[17]

It may be tempting to utilize the TE model (ii) to describe the forward bias characteristics. This model (ii) is given by

$$J_{TE} = J_0\left[\exp\left(-\frac{qV_F}{nk_B T}\right) - 1\right],$$
$$J_0 = A_R T^2 \exp\left(-\frac{q\phi_B - \Delta\phi_{IFL}}{k_B T}\right), \tag{12}$$

with ideality *n*.[47] For this TE model, *n* and ϕ_B are the two free parameters and extracted by fitting Eq. (12) to the data plotted in Fig. 10(a). The Schottky barrier obtained from this TF model is given in Table I and significantly lower than $\phi_{B,TFE}$ obtained by the TFE model. This reduction arises because tunneling effects are not included in the TE model and this approach can usually be applied when E_{surf} is low.[40] Due to the large N_d, the resulting E_{surf} at zero bias is high and image-force-lowering [Eq. (8)] must not be neglected to extract ϕ_B for our PtO/β-Ga_2O_3 device structure.[19]

The voltage (V_T) at which the TFE currents dominate over TE currents can now be determined as[45]

$$V_T = \phi_B + \xi - \frac{3}{2}E' \frac{\cosh^2\left(\frac{E'}{k_B T}\right)}{\sinh^3\left(\frac{E'}{k_B T}\right)}, \tag{13}$$

with the correction for band-filling effects, ξ.[45] Note, Smith *et al.* corroborates that the TFE currents may dominate for $N_d \propto 10^{18}$ cm^{-3} even at $T \approx 300$ K as long as the Schottky barrier exceeds several times of $k_B T$, i.e., for $\phi_B \gg k_B T$.[48] For the PtO/β-Ga_2O_3 diodes, this transition voltage to TE-dominated current exceeds $V_T > 1.75$ V, under all conditions.

We next extract ϕ_B by reverse leakage current–field (*J*–*E*) measurements. We apply the numeric tunneling model developed by Li *et al.*[19] to the data shown in Fig. 11(a). In this model, the total reverse leakage current is given by[49]

$$J = \frac{A_R T}{k_B}\int_{\mathcal{E}_{min}}^{+\infty} \mathcal{T}(\mathcal{E}) \times \ln\left[1 + \exp\left(-\frac{\mathcal{E} - \mathcal{E}_{FM}}{k_B T}\right)\right] d\mathcal{E}, \tag{14}$$

where $\mathcal{E}$ is the electron energy, $\mathcal{E}_{min}$ the minimum energy for a tunneling process to occur, $\mathcal{T}(\mathcal{E})$ is the transmission probability across the Schottky barrier, and $\mathcal{E}_{FM}$ is the Fermi energy in metal (M). Setting $\mathcal{E}_{FM}$ to the zero-energy level and assuming non-negligible image-force lowering (i.e., $\Delta\phi_{IFL} > 0$), the potential energy of the Schottky barrier is

$$\mathcal{E}_c(x) = q\phi_B - qE_{surf}\,x - \frac{q^2}{16\pi\varepsilon_s}\frac{1}{x} + \frac{q^2 N_d}{2\varepsilon_s}x^2. \tag{15}$$

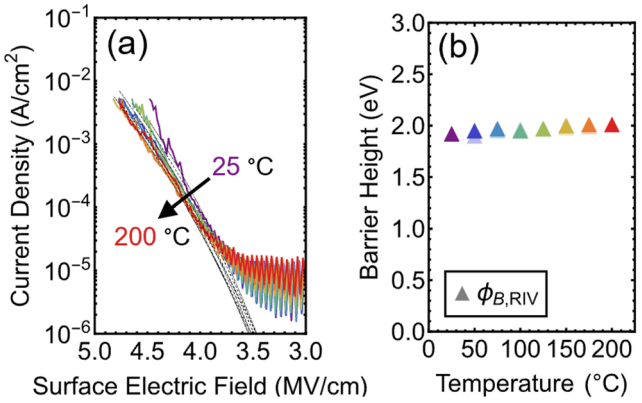

FIG. 11. (a) *T*-dependent reverse leakage current density as a function of the surface electric field (E_{surf}) of our PtO/β-Ga_2O_3 Schottky diodes (*J*–*E* characteristics). The numerical tunneling model is fit to these data, Eq. (14). (b) Extracted ϕ_B as a function of *T* yield stable values on heating (solid symbols) and cooling (opaque symbols). The color of the *T*-dependent data plotted in (a) follows the corresponding temperature color scale used in (b).

Using the Wentzel–Kramers–Brillouin approximation,[50,51] the transmission probability converts to

$$\mathcal{T}(\mathcal{E}) = \begin{cases} \left[1 + \exp\left(-\frac{2i}{\hbar}\int_{x_1}^{x_2} p(x)\mathrm{d}x\right)\right]^{-1}, & \mathcal{E} \le \mathcal{E}_{c,max} \\ 1, & \mathcal{E} > \mathcal{E}_{c,max} \end{cases} \quad (16)$$
$$p(x) = -i\sqrt{2m^*((\mathcal{E}_c(x) - \mathcal{E}))},$$

with effective mass $m^* \approx 0.31_0$ for β-Ga_2O_3[52] and the classical turning points $p(x)$, x_1, and x_2 at $\mathcal{E}_c = \mathcal{E}$.[19] As N_d has been extracted from the C–V data in Fig. 9, ϕ_B is the only free parameter in Eq. (14) for numerically fitting the data given in Fig. 11(a). The resulting Schottky barrier height extracted from reverse J–E measurements is given in Table I. Despite the initial stability in leakage current, exhibited by the room temperature J–E measurement in Fig. 11(a), extracted values on heating and cooling did not vary significantly.

To finally quantify ϕ_B for the PtO/β-Ga_2O_3 structure and models used, we take the mean and its deviation of $\phi_{B,CV}$, $\phi_{B,TFE}$, and $\phi_{B,RIV}$, provided in Table I. Note, we neglect $\phi_{B,TE}$ because our obtained N_d (and thus E_{surf}) are too large to neglect tunneling in the model. We then obtain $\phi_B^{avg} = (2.23 \pm 0.18)$ eV. Our results indicate that despite only reaching surface electric fields of $E_{surf} \approx 4.4$ MV cm^{-1} at a leakage current of 1 mA cm^{-2}, no permanent modification in the properties of the PtO anode was observed. This surface electric field exceeds the typical critical electric fields for SiC and GaN of $E_{surf} \approx 2.5$ MV cm^{-1}.[53,54] Further growth and process optimization, for example, oxide field plate or passivation, may reduce instability in the future PtO/β-Ga_2O_3 devices to reach $E_{surf} > 6$ MV cm^{-1} at a leakage current of 1 mA cm^{-2}.[19]

We note that significant additional study is needed to fully utilize tetragonal PtO as an anode contact on β-Ga_2O_3 for competitive kV-power devices. For example, the quality of the PtO anode must be maintained through required energetic processing or those which require elevated process temperatures, such as rapid thermal annealing (RTA) for ohmic contact formation. Moreover, the highly oxidizing deposition conditions must not degrade or negatively impact the β-Ga_2O_3 channel nor other previously formed device structures. For rectifiers, it is likely that a junction barrier Schottky-like (JBSD) or merged P-i-N Schottky-like (MPS) structure must be utilized to offset the high turn on voltage in on-state operation. With lack of a selective etch chemistry, the PtO must be removed by energetic ion-milling, which is likely to damage the underlying β-Ga_2O_3 and increase the likelihood of unintentional reduction at the newly revealed PtO surfaces. We believe these challenges are each on their own achievable and that our initial work promises the potential of tetragonal PtO to be used as an anode in high-power β-Ga_2O_3 devices.

IV. CONCLUSIONS

Since its prediction in 1941, the existence of tetragonal PtO has been debated. Using ozone MBE, we have now accomplished the epitaxial growth of tetragonal PtO (space group: $P4_2/mmc$) on MgO, TiO_2, and β-Ga_2O_3 substrates. We identified the growth window of PtO on all three substrates by compiling an MBE P–T_G diagram. Our results agree with thermodynamics, and our PtO growth is limited by the maximum applicable ozone pressure (p_{O_3}) in our MBE system.[26] We note that the emerging thermal laser epitaxy (TLE) film growth method can expand the parameter space under which previously inaccessible materials can be grown[55,56] including the PtO noble-metal oxide in this work.

Using PtO grown on MgO and TiO_2, we performed electrical, Hall, photoemission, and optical measurements. In conjunction with density functional theory calculations, our analysis reveals PtO to be a degenerately doped p-type semiconductor with a bandgap of $E_a \approx 1.6$ eV. We speculate that p-type conductivity in tetragonal PtO emerges due to an excess of oxygen in our PtO films, i.e., $PtO_{1+\delta}$.

Using PtO grown on n-type β-Ga_2O_3, we fabricated Schottky diodes and extracted its Schottky barrier height (ϕ_B) using different approaches and models and obtain $\phi_B = (2.23 \pm 0.18)$ eV. Such high barriers are needed to reach the critical electric field in β-Ga_2O_3-based Schottky diodes of $E_{crit} > 6$ MV cm^{-1} at leakage currents of 1 mA cm^{-2}[19,21,40] The apparent surface electric field at the PtO/β-Ga_2O_3 interface exceeded $E_{surf} > 4.4$ MV cm^{-1} at a leakage current of 1 mA cm^{-2} before premature breakdown of the Schottky diode emerged. This hints that yield and statistics of our PtO/β-Ga_2O_3 Schottky interface require optimization in growth and processing. Nevertheless, our epitaxial PtO thin films grown at back-end-of-line compatible (BEOL) temperatures[57] are a testament to the potential use of noble-metal-oxides for high-power Ga_2O_3 Schottky Diodes.

SUPPLEMENTARY MATERIAL

See the supplementary material for additional information on RHEED and XRD data of PtO(100)/β-Ga_2O_3(010) (Fig. S1), crystallographic data, transport data (Fig. S2), XPS measurements (Fig. S3), and photoemission data and more details on band structure, ARPES data, and DFT calculations (Figs. S4–S7).

ACKNOWLEDGMENTS

The work at Cornell University was primarily supported by the AFOSR/AFRL ACCESS Center of Excellence under Award No. FA9550-18-1-0529. This work made use of the thin film synthesis facility of the Platform for the Accelerated Realization, Analysis, and Discovery of Interface Materials (PARADIM) for MBE+ARPES, which is supported by the National Science Foundation under Cooperative Agreement No. DMR-2039380. Our work also used the Cornell Center for Materials Research (CCMR) Shared Facilities, which are supported through the NSF MRSEC Program (Grant No. DMR-1719875). Substrate preparation was performed partially using the Cornell NanoScale Facility, a member of the National Nanotechnology Coordinated Infrastructure (NNCI), which was supported by the NSF (Grant No. NNCI-2025233).

AUTHOR DECLARATIONS

Conflict of Interest

The authors have no conflicts to disclose.

Author Contributions

Felix V. E. Hensling: Conceptualization (equal); Data curation (equal); Investigation (equal); Methodology (equal); Writing – original draft (equal). **Christopher T. Parzyck**: Conceptualization (equal); Data curation (equal); Investigation (equal); Methodology (equal); Validation (equal); Writing – original draft (equal); Writing – review & editing (supporting). **Bennett Cromer**: Conceptualization (supporting); Data curation (equal); Investigation (equal); Methodology (equal); Validation (equal); Writing – original draft (equal); Writing – review & editing (supporting). **Md. Abdullah Al Mamun**: Conceptualization (supporting); Formal analysis (equal); Investigation (equal); Methodology (equal). **Y. Eren Suyolcu**: Investigation (equal); Methodology (equal); Visualization (supporting). **L. Kalaydjian**: Formal analysis (equal); Methodology (equal); Visualization (supporting). **Indra Subedi**: Formal analysis (supporting); Methodology (supporting). **Jisung Park**: Formal analysis (supporting); Methodology (supporting). **Kathy Azizie**: Data curation (supporting). **Qi Song**: Methodology (supporting). **Peter A. van Aken**: Formal analysis (supporting); Methodology (equal); Resources (equal). **Nikolas J. Podraza**: Conceptualization (equal); Data curation (equal); Formal analysis (equal); Investigation (equal); Writing – original draft (equal). **Kyeongjae Cho**: Conceptualization (equal); Formal analysis (supporting); Investigation (supporting); Resources (equal). **Debdeep Jena**: Funding acquisition (equal); Methodology (equal); Resources (equal). **Huili G. Xing**: Conceptualization (equal); Funding acquisition (equal); Methodology (equal); Resources (equal). **Kyle M. Shen**: Conceptualization (equal); Funding acquisition (equal); Methodology (equal); Resources (equal). **Darrell G. Schlom**: Conceptualization (lead); Funding acquisition (lead); Investigation (equal); Project administration (lead); Resources (lead); Supervision (lead); Writing – review & editing (lead). **Patrick Vogt**: Conceptualization (lead); Formal analysis (equal); Investigation (lead); Methodology (equal); Project administration (equal); Writing – original draft (lead); Writing – review & editing (lead).

DATA AVAILABILITY

The data that support the findings of this study are available within the article and its supplementary material. Additional data related to the film growth (MBE growth logs) and structural characterization by RHEED, XRD, XPS, transport data, ARPES, and DFT calculations are available at https://doi.org/10.34863/6391-0w29. Any additional data connected to the study are available from the corresponding author upon reasonable request.

APPENDIX: EXPERIMENTAL DETAILS

1. MBE growth system

Epitaxial PtO was grown in an Veeco GEN10 MBE system, and platinum was supplied during growth using an *e*-beam evaporator or a high-temperature effusion cell. The platinum flux was set to $\phi_{Pt} \sim 1 \times 10^{13}$ cm^{-2} s^{-1} and calibrated by growing metallic platinum and performing subsequent x-ray reflectivity (XRR) measurements.[58] From this flux, the resulting growth rate of tetragonal PtO was $\Gamma \sim 10$ nm h^{-1}. High quality PtO films were grown with thicknesses ranging between 10 and 130 nm. The 10×10 mm^2 substrates were back-side coated with a 10 nm thick titanium adhesion layer followed by 200 nm of platinum, enabling the otherwise transparent substrates to be radiatively heated during MBE growth. The substrates were cleaned *ex situ* with isopropanol. The substrate was held within a substrate holder made of Haynes® 214® alloy and loaded into the growth chamber. The growth temperature (T_G) was measured by an optical pyrometer operating at a wavelength of 1550 nm. The substrates were annealed under vacuum ($\sim 10^{-9}$ mbar) at $T_G = 800\,^{\circ}$C until the expected surface crystallinity and quality of the used substrates emerged, and measured *in situ* by high-energy electron diffraction (RHEED) using 13 keV electrons. To determine the surface crystal phases during the growth of the films, we also used *in situ* RHEED measurements. After growth, XRR and x-ray diffraction (XRD) were used to identify the growth of tetragonal PtO and to determine its thickness and epitaxial orientation relationship, using a four-circle x-ray diffractometer with Cu Kα_1 radiation.

2. Scanning transmission electron microscopy

For the electron-transparent TEM specimen, a standard sample preparation procedure was performed, including mechanical grinding and tripod wedge polishing (Multiprep, Allied HighTech) and argon ion milling with a liquid nitrogen cooled stage (PIPS II, Model 695). High-angle annular dark-field scanning transmission electron microscopy (STEM-HAADF) data were acquired using a probe aberration-corrected JEOL JEM-ARM200F scanning transmission electron microscope equipped with a cold-field emission electron source and a probe Cs corrector (DCOR, CEOS GmbH) at 200 kV. STEM-HAADF imaging was performed with a convergence semi-angle of 20 mrad, resulting in a probe size of 0.8 Å. The collection angles for the HAADF images ranged from 75 to 310 mrad.

3. Electrical transport

Temperature-dependent resistivity, magnetoresistance, and Hall resistance measurements were performed using a Quantum Design Physical Property Measurement System (PPMS) with a base temperature of 2 K and an out-of-plane magnetic field varying between $H = -7$ T and $H = +7$ T. Electrical contacts were prepared using ultrasonic aluminum wirebonding. For determination of ρ_{xx}, electrical transport was measured in a linear four-point geometry with a typical lead spacing of 750 μm, and finite size effects were accounted for using the methods described in Ref. 59. Measurements were performed along both in-plane directions with no significant or systematic differences between the two directions observed. Measurements of ρ_{xy} were performed using a square geometry with electrical leads placed on the four corners of the 10×10 sample; measurements of both ρ_{xy} and ρ_{yx} were performed and found to be in agreement, and estimates of the 3D carrier density and mobility were obtained by linear fitting of $\rho_{xy}(H)$ and applying a single band model.

4. Photoemission spectroscopy measurements

ARPES measurements were performed on PtO(011)/TiO$_2$(110) films using a Fermion Instruments BL1200s Helium discharge lamp generating He-I ($h\nu = 21.2$ eV) and He-II ($h\nu = 40.8$ eV) light along with a Scienta Omicron R8000 electron analyzer. Samples were

cooled to a temperature of $T = 20$ K for measurement using a liquid helium cryostat affixed to a custom built motorized six-axis manipulator with a temperature sensor built into the stage. The nominal system energy and angular resolutions were set to 20 meV and 0.4°, respectively; the Fermi level was measured using a gold reference electrically connected to the sample. The measurements presented in the text were performed on a sample, which was removed from vacuum for a short period following growth, reintroduced, and annealed in a background pressure of $P = 3 \times 10^{-6}$ Torr of distilled ozone at a temperature of $T = 310$ °C (measured by optical pyrometer operating at a wavelength of 1550 nm) until clear RHEED streaks were observed. The sample was then immediately transferred through an adjoined vacuum manifold ($P_{base} < 2 \times 10^{-11}$ Torr) to the measurement chamber ($P_{base} < 3.5 \times 10^{-11}$ Torr). Additional measurements were performed on several other samples which were transferred immediately and directly between the growth and analysis chambers in ultra-high vacuum; identical dispersive features were observed in both *in situ* and *ex situ* transferred samples.

Ex situ x-ray photoemission spectroscopy measurements were performed on a PtO(100)/MgO(001) film using a Thermo Scientific Nexsa G2 XPS system utilizing a non-monochromated Al Kα source ($h\nu = 1486.8$ eV). Survey spectra were collected at an electron pass energy of 200 eV and higher resolution scans of selected peaks were performed using a pass energy of 50 eV. Both the PtO thin film and platinum reference film were measured at the same time under the same conditions and were electrically connected to a common ground; the Fermi energy was calibrated using the Fermi step of the platinum reference sample which gives consistent value of 284.75 eV for the carbon 1*s*-peak in both samples.

5. Density functional theory calculations

Theoretical calculations were performed by using DFT as implemented in Vienna *Ab Initio* Simulation Package (VASP) with the projected augmented wave (PAW) scheme.[60,61] To gain better understanding of the bandgap (E_a) and electronic structure of PtO, the hybrid functional developed by Heyd, Scuseria, and Ernzerhof (HSE) was employed with mixing parameter $\alpha = 0.33$ for exact exchange and combined with the semilocal Perdew–Burke–Ernzerhof generalized gradient approximation.[62,63] Geometric relaxations were carried out until the force on each atom in the primitive unit cell is reduced to less than 50 meV Å^{-1}. Electronic minimization were performed using a $10 \times 10 \times 6$ Monkhorst–Pack *k*-point sampling, with a cutoff energy of 520 eV and an energy convergence criterion of 10^{-6} eV.

6. Spectroscopic ellipsometry

Ellipsometric spectra in terms of $N = \cos 2\psi$, $C = \sin 2\psi \cos \Delta$, and $S = \sin 2\psi \sin \Delta$ were collected for epitaxial PtO on single crystalline MgO, PtO capped with MgO on single crystalline MgO, and for as-grown PtO films. The ellipsometric quantities $\tan \psi$ and Δ are the relative amplitude ratio and phase shift difference, respectively, for electric fields polarized parallel and perpendicular to the plane of incidence of the specimens. Reflection-mode measurements at 50°, 60°, and 70° angles of incidence over a spectral range of 0.75–0.95 eV were performed using a single rotating compensator multichannel ellipsometer (J. A. Woollam M-2000).[64,65] Structural and optical models were fit to the measured ellipsometric spectra using least squares regression with an unweighted error function.[66]

To analyze the data plotted in Fig. 7, we use the following expression:[33,34,37]

$$\begin{aligned} \epsilon &= \epsilon_\infty + \epsilon_S + \epsilon_D + \epsilon_L, \quad \text{with} \\ \epsilon_S &= \frac{A}{E_0^2 - E^2}, \\ \epsilon_D &= \frac{\hbar^2}{\epsilon_0 \rho \left(\tau E^2 + i\hbar E\right)}, \\ \epsilon_L &= \sum_n \frac{\mathcal{A}_n \Gamma_n E_0^n}{\left((E_0^n)^2 - E^2\right) - i\Gamma_n E}. \end{aligned} \tag{A1}$$

For the Sellmaier expression (ϵ_S), A is the amplitude and E_0 is the resonance energy. For the Drude expression (ϵ_D), $\hbar$ is the reduced Planck constant, ϵ_0 is the vacuum permittivity, ρ is the resistivity, and τ is the scattering time. For each Lorentz oscillator (ϵ_L), $\mathcal{A}_n$ are the amplitudes, Γ_n are their broadening, and E_0^n are the resonance energies. Equation (A1) is applied to the data shown in Fig. 7 and obtained parameters are provided in Table III.

7. Processing of Schottky diodes

To fabricate vertical Schottky diodes, the MBE-grown Pt/PtO/β-Ga_2O_3 structure was first solvent cleaned in acetone and isopropanol. After removing excess water vapor by dehydrating the sample at 180 °C, an additional 100 nm of platinum was deposited by *e*-beam evaporation on the Pt/PtO surface to provide a mechanically robust contact for electrical probing. Evaporation was performed in a CVC SC-4500 evaporation system at an operational pressure of 1×10^{-6} Torr at 1 Å s^{-1}.

Subsequently, a 3 μm thick photomask of Microposit® S1827 was spun on and exposed for 800 ms within an *i*-line GCA AS200 AutoStep exposure system. After pattern development in metal-ion-free AZ726 developer for 60 s, the sample was loaded into an AJA International 2036 Ion Milling System. The etch process utilized ionized Ar^+ with an accelerating voltage of 600 V, resulting in a mesa step height of 300 nm after photoresist removal in Microposit Remover 1165, as shown in Fig. 8. As demonstrated in prior studies,[18] a 300 nm mesa structure is sufficient edge termination to yield ideal current characteristics at high doping densities on the order of 10^{18} cm^{-3}.[18,19,67]

Electrical characteristics were captured with a Keithley 4200A-SCS Parameter Analyzer connected to a Signatone Checkmate high-stability 200 mm manual probe station. This probe station utilized an ATT A200H Control Unit for resistive heating of the chuck with

TABLE II. Fitting parameters describing the ellipsometric spectra collected for single-crystal MgO. The surface layer thickness is $d = (1.98 \pm 0.02)$ nm and $\epsilon_\infty = 1.5 \pm 0.1$. The quality of fit is expressed by the mean squared error, MSE = 3.7×10^{-3}.

Sellmaier	Res. ener., E_0 (eV)	Amp., A (eV^2)
	10.0 ± 0.2	145 ± 0.14

TABLE III. Fitting parameters describing the multiple sample analysis of ellipsometric spectra collected for two uncapped and two MgO-capped PtO films with $\epsilon_\infty = 1.18 \pm 0.08$ and MSE = 9.2×10^{-3}. Samples S1 and S2 are PtO films with thicknesses $d_{S1} \approx 34$ nm and $d_{S2} \approx 37$ nm, respectively. Samples S3 and S4 are MgO-capped plus PtO films with total thicknesses $d_{S3} \approx 17$ nm MgO + 38 nm MgO and $d_{S2} \approx 27$ nm MgO + 53 nm PtO, respectively.

Drude	Resistivity, ρ (mΩ cm)		Scatt. time, τ (ps)
	0.74 ± 0.01		330 ± 5
Lorentz	Res. ener., E_0 (eV)	Amp., $\mathcal{A}$	Broad., Γ (eV)
1	4.03 ± 0.01	6.10 ± 0.20	2.02 ± 0.04
2	3.04 ± 0.01	2.73 ± 0.09	0.88 ± 0.03
3	2.26 ± 0.01	0.78 ± 0.03	0.51 ± 0.03
3	7.30 ± 0.30	2.42 ± 0.04	7.00 ± 1.00
Sellmaier	Res. ener., E_0 (eV)		Amp., A (eV^2)
	7.49 ± 0.07		59 ± 0.20

a temperature stability of $\Delta T \pm 0.1$ K. In this configuration, the system yielded a noise floor less than 200 pA and 15 fF for all T and measurements.

REFERENCES

[1] W. J. Moore, Jr. and L. Pauling, J. Am. Chem. Soc. **63**, 1392 (1941).
[2] E. E. Galloni and A. E. Roffo, Jr., J. Chem. Phys. **9**, 875 (1941).
[3] O. Muller and R. Roy, J. Less-Common Met. **16**, 129 (1968).
[4] M. P. H. Fernandez and B. L. Chamberland, J. Less-Common Met. **99**, 99 (1984).
[5] A. N. Mansour, D. E. Sayers, J. W. Cook, Jr., D. R. Short, R. D. Shannon, and J. R. Katzer, J. Phys. Chem. **88**, 1778 (1984).
[6] R. K. Nomiyama, M. J. Piotrowski, and J. L. F. Da Silva, Phys. Rev. B **84**, 100101 (2011).
[7] K. P. Kepp, Chem. Phys. Chem. **21**, 360 (2020).
[8] N. Seriani and F. Mittendorfer, J. Phys. Condens. Matter **20**, 184023 (2008).
[9] B. J. Baliga, J. Appl. Phys. **53**, 1759 (1982).
[10] B. J. Baliga, IEEE Electron Device Lett. **10**, 455 (1989).
[11] B. J. Baliga, *Fundamentals of Power Semiconductor Devices*, 1st ed. (Springer Publishing Company, Incorporated, 2008).
[12] J. Y. Tsao, S. Chowdhury, M. A. Hollis, D. Jena, N. M. Johnson, K. A. Jones, R. J. Kaplar, S. Rajan, C. G. Van de Walle, E. Bellotti, C. L. Chua, R. Collazo, M. E. Coltrin, J. A. Cooper, K. R. Evans, S. Graham, T. A. Grotjohn, E. R. Heller, M. Higashiwaki, M. S. Islam, P. W. Juodawlkis, M. A. Khan, A. D. Koehler, J. H. Leach, U. K. Mishra, R. J. Nemanich, R. C. N. Pilawa-Podgurski, J. B. Shealy, Z. Sitar, M. J. Tadjer, A. F. Witulski, M. Wraback, and J. A. Simmons, Adv. Electron. Mater. **4**, 1600501 (2018).
[13] M. Higashiwaki, K. Sasaki, H. Murakami, Y. Kumagai, A. Koukitu, A. Kuramata, T. Masui, and S. Yamakoshi, Semicond. Sci. Technol. **31**, 031001 (2016).
[14] K. Ghosh and U. Singisetti, J. Appl. Phys. **124**, 085707 (2018).
[15] Z. Galazka, J. Appl. Phys. **131**, 031103 (2022).
[16] M. Mohamed, K. Irmscher, C. Janowitz, Z. Galazka, R. Manzke, and R. Fornari, Appl. Phys. Lett. **101**, 132106 (2012).
[17] C. Hou, R. M. Gazoni, R. J. Reeves, and M. W. Allen, Appl. Phys. Lett. **114**, 033502 (2019).
[18] B. Cromer, D. Saraswat, N. Pieczulewski, W. Li, K. Nomoto, F. V. E. Hensling, K. Azizie, H. P. Nair, D. G. Schlom, D. A. Muller, D. Jena, and H. G. Xing, J. Vac. Sci. Technol., A **42**, 033206 (2024).
[19] W. Li, D. Saraswat, Y. Long, K. Nomoto, D. Jena, and H. G. Xing, Appl. Phys. Lett. **116**, 192101 (2020).
[20] E. Farzana, A. Bhattacharyya, N. S. Hendricks, T. Itoh, S. Krishnamoorthy, and J. S. Speck, APL Mater. **10**, 111104 (2022).
[21] W. Li, K. Nomoto, M. Pilla, M. Pan, X. Gao, D. Jena, and H. G. Xing, IEEE Trans. Electron Devices **64**, 1635 (2017).
[22] E. Farzana, S. Roy, N. S. Hendricks, S. Krishnamoorthy, and J. S. Speck, Appl. Phys. Lett. **123**, 192102 (2023).
[23] P. Schlupp, D. Splith, H. von Wenckstern, and M. Grundmann, Phys. Status Solidi A **216**, 1800729 (2019).
[24] Y. Jia, S. Sato, A. Traoré, R. Morita, E. Broccoli, F. F. Florena, M. M. Islam, H. Okumura, and T. Sakurai, AIP Adv. **13**, 105306 (2023).
[25] J. Wan, H. Wang, C. Zhang, Y. Li, C. Wang, H. Cheng, J. Li, N. Ren, Q. Guo, and K. Sheng, Appl. Phys. Lett. **124**, 243504 (2024).
[26] S.-L. Shang, S. Lin, M. C. Gao, D. G. Schlom, and Z.-K. Liu, APL Mater. **12**, 081110 (2024).
[27] Y. Krockenberger, J. Kurian, A. Winkler, A. Tsukada, M. Naito, and L. Alff, Phys. Rev. B **77**, 060505 (2008).
[28] H. P. Nair, Y. Liu, J. P. Ruf, N. J. Schreiber, S.-L. Shang, D. J. Baek, B. H. Goodge, L. F. Kourkoutis, Z.-K. Liu, K. M. Shen, and D. G. Schlom, APL Mater. **6**, 046101 (2018).
[29] V. G. Tsirelson, A. S. Avilov, Y. A. Abramov, E. L. Belokoneva, R. Kitaneh, and D. Feil, Acta. Cryst. B **54**, 8 (1998).
[30] H. J. T. Ellingham, Chem. Ind. **63**, 125 (1944).
[31] H. Kiessig, Ann. Phys. **402**, 769 (1931).
[32] D. Hong, C. Liu, L. Wang, J. Wen, J. E. Pearson, and A. Bhattacharya, Phys. Rev. Mater. **5**, 044205 (2021).
[33] W. v. Sellmeier, Ann. Phys. **219**, 272 (1871).
[34] R. W. Collins and A. S. Ferlauto, *Handbook of Ellipsometry* (William Andrew, Norwich, NY, 2005), p. 125.
[35] D. E. Aspnes, J. B. Theeten, and F. Hottier, Phys. Rev. B **20**, 3292 (1979).
[36] H. Fujiwara, J. Koh, P. I. Rovira, and R. W. Collins, Phys. Rev. B **61**, 10832 (2000).
[37] T. E. Tiwald, D. W. Thompson, J. A. Woollam, W. Paulson, and R. Hance, Thin Solid Films **313**, 661 (1998).
[38] W. G. Oldham, Surf. Sci. **16**, 97 (1969).
[39] P. Uprety, M. M. Junda, K. Ghimire, D. Adhikari, C. R. Grice, and N. J. Podraza, Appl. Surf. Sci. **421**, 852 (2017).
[40] W. Li, D. Jena, and H. G. Xing, J. Appl. Phys. **131**, 015702 (2022).
[41] F. A. Padovani and G. G. Sumner, J. Appl. Phys. **36**, 3744 (1965).
[42] B. Hoeneisen, C. A. Mead, and M.-A. Nicolet, Solid-State Electron. **14**, 1057 (1971).
[43] W. Mönch, J. Vac. Sci. Technol., B **17**, 1867 (1999).
[44] C. R. Crowell, Solid-State Electron. **8**, 395 (1965).

[45]F. A. Padovani and R. Stratton, Solid-State Electron. **9**, 695 (1966).
[46]M. Passlack, N. E. J. Hunt, E. F. Schubert, G. J. Zydzik, M. Hong, J. P. Mannaerts, R. L. Opila, and R. J. Fischer, Appl. Phys. Lett. **64**, 2715 (1994).
[47]C. Herring and M. H. Nichols, Rev. Mod. Phys. **21**, 185 (1949).
[48]K. T. Smith, C. A. Gorsak, J. T. Buontempo, B. J. Cromer, T. Ikenoue, H. Gulupalli, M. O. Thompson, D. Jena, H. P. Nair, and H. G. Xing, J. Appl. Phys. **136**, 215302 (2024).
[49]E. L. Murphy and R. H. Good, Phys. Rev. **102**, 1464 (1956).
[50]G. Wentzel, Z. Phys. **38**, 518 (1926).
[51]H. A. Kramers, Z. Phys. **39**, 828 (1926).
[52]Y. Zhang, A. Neal, C. Joishi, J. M. Johnson, Y. Zheng, S. Bajaj, M. Brenner, D. Dorsey, K. Chabak, G. Jessen, J. Hwang, S. Mou, J. P. Heremans, and S. Rajan, Appl. Phys. Lett. **112**, 173502 (2018).
[53]A. O. Konstantinov, Q. Wahab, N. Nordell, and U. Lindefelt, Appl. Phys. Lett. **71**, 90 (1997).
[54]T. Maeda, T. Narita, S. Yamada, T. Kachi, T. Kimoto, M. Horita, and J. Suda, J. Appl. Phys. **129**, 185702 (2021).
[55]F. V. E. Hensling, W. Braun, D. Y. Kim, L. N. Majer, S. Smink, B. D. Faeth, and J. Mannhart, APL Mater. **12**, 040902 (2024).
[56]L. N. Majer, T. Acartürk, P. A. Aken, W. Braun, L. Camuti, J. Eckl-Haese, J. Mannhart, T. Onuma, K. S. Rabinovich, D. G. Schlom, S. Smink, U. Starke, J. Steele, P. Vogt, H. Wang, and F. V. E. Hensling, APL Mater. **12**, 091112 (2024).
[57]F. V. E. Hensling, P. Vogt, J. Park, S.-L. Shang, H. Ye, Y.-M. Wu, K. Smith, V. Show, K. Azizie, H. Paik, D. Jena, H. G. Xing, Y. E. Suyolcu, P. A. van Aken, S. Datta, Z.-K. Liu, and D. G. Schlom, Adv. Electron. Mater. **11**, 2400499 (2025).
[58]J. Sun, C. T. Parzyck, J. H. Lee, C. M. Brooks, L. F. Kourkoutis, X. Ke, R. Misra, J. Schubert, F. V. Hensling, M. R. Barone, Z. Wang, M. E. Holtz, N. J. Schreiber, Q. Song, H. Paik, T. Heeg, D. A. Muller, K. M. Shen, and D. G. Schlom, Phys. Rev. Mater. **6**, 033802 (2022).
[59]I. Miccoli, F. Edler, H. Pfnür, and C. Tegenkamp, "The 100th anniversary of the four-point probe technique: The role of probe geometries in isotropic and anisotropic systems," J. Phys.: Condens. Matter **27**, 223201 (2015).
[60]G. Kresse and J. Hafner, Phys. Rev. B **47**, 558 (1993).
[61]G. Kresse and J. Furthmüller, Phys. Rev. B **54**, 11169 (1996).
[62]J. P. Perdew, K. Burke, and M. Ernzerhof, Phys. Rev. Lett. **77**, 3865 (1996).
[63]J. Heyd, G. E. Scuseria, and M. Ernzerhof, J. Chem. Phys. **118**, 8207 (2003).
[64]J. Lee, P. I. Rovira, I. An, and R. W. Collins, Rev. Sci. Instrum. **69**, 1800 (1998).
[65]J. A. Woollam, B. D. Johs, C. M. Herzinger, J. N. Hilfiker, R. A. Synowicki, and C. L. Bungay, "Very high parallel-plane surface electric field of 4.3 MV/cm in Ga_2O_3 Schottky barrier diodes with PtO_x contacts," Proc. SPIE **10294**, 1029402 (1999).
[66]B. Johs and C. M. Herzinger, Phys. Status Solidi C **5**, 1031 (2008).
[67]D. Saraswat, W. Li, K. Nomoto, D. Jena, and H. G. Xing, "Very high parallel-plane surface electric field of 4.3 MV/cm in Ga_2O_3 Schottky barrier diodes with PtO_x contacts," in *2020 Device Research Conference (DRC)* (IEEE, 2020), pp. 1–2.
[68]Y. Li, J. Xia, and V. Srivastava, Front. Chem. **8**, 704 (2020).